ADVANCED THEORY AND SIMULATIONS
www.advtheorysimul.com

Enhanced Photon Harvesting in Wedge Tandem Solar Cell

Sandeep Kumar Chamoli, Subhash Singh, Chunlei Guo,* and Wei Li**

Light-trapping elements play an important role in solar cells to enhance their light-harvesting efficiency. Pyramidal-shaped nano-microstructures and gradient metasurfaces are mostly used as light-trapping elements in solar cells. There is, however, one major concern with nanostructured solar cells: a larger surface area resulting in a larger surface recombination loss. In this article, a novel thin-film wedge tandem-solar cell made of perovskites and silicon is designed where the bottom cell itself works as a light-trapping element. Optical and electrical simulations are performed to estimate performance metrics of the wedge tandem-solar cell and compare with typically used unpatterned planar tandem-solar cell. In terms of optical and electrical performance, wedge geometry outperforms planar geometry and shows 17.18% higher efficiency. Compared to a typical planar tandem cell, such a design can lead to thin and low-weight tandem solar cells, which can be very useful in space applications. The proposed design can be fabricated using an optimized electrospray deposition process.

1. Introduction

Solar energy is a promising low-cost alternative to fossil fuels that has the potential to meet the ever-increasing global energy demands. The total annual solar energy reaching the earth's surface is about 7500-fold of the annual global energy consumption of about 125 petawatt-hours.[1,2] Solar photovoltaic (PV) is the most efficient and popular way that directly converts solar energy into useful electricity. Silicon (Si), cadmium telluride (CdTe), gallium arsenide (GaAs), copper indium gallium selenide (CIGS), and perovskites are commonly used PV materials. Due to the huge abundance of silicon, its nontoxic nature, low cost, strong photostability, long lifetime, and mature fabrication technology, single-junction silicon PV cells dominate over others and capture ≈90% of the current PV solar cells market.[2] Among all emerging PV materials, perovskites have recently demonstrated fast growth and achieved up to 25.2% efficiency in a short period.[3] The optimal thickness of a given PV material is a trade-off between high optical absorption and an efficient photocarrier collection. For example, optical absorption increases with the thickness of the material, but a thicker PV material possesses larger carrier recombination. Therefore, theoretical efficiency for a single-junction solar cell is limited to Shockley–Queisser (SQ) limit which is about 33.7%.[4]

Thin-film solar cells are comparatively lightweight, low-cost, and easily z.[5] These cells even could have a higher efficiency if an efficient light-trapping mechanism is realized. Therefore, various light-trapping strategies are developed to push the efficiency of single-junction thin-film PV cells toward the SQ limit.[6] These light-trapping schemes restrict light to oscillate multiple rounds in a thin active medium. Yablonovitch and Cody demonstrated the versatility of light trapping in a thin film using statistical mechanics and ray optics.[7] The analysis reveals that the intensity of confined light in a non-absorbing active medium can be even larger than the intensity of incident light itself. Light-trapping strategies enhance optical absorption in a broad spectral region resulting in highly efficient, thinner, and low-cost solar cells and photodetectors.[8] Nano-photonic structures and diffractive gratings are efficient light-trapping elements that effectively reduce surface reflection by minimizing the refractive index mismatch and increasing the optical path length through oscillations of light in the cavity.[9–11] Multi-junction and tandem PV cells are developed to overcome the single-junction SQ limit.[12] Spectral splitting is the key to achieving high conversion efficiencies in these cells.[8,10,13] In a typical tandem solar cell, the incident light is spectrally split between the upper and lower cells. The upper cell, typically made of a relatively wider bandgap material, absorbs higher energy photons and allows transmission of the lower energy photons to the bottom cell made of a narrow bandgap material. Through an intelligent selection of materials, the number of layers, and the design of an efficient optical cavity, photons from the entire solar spectrum can be efficiently harvested. This strategy can also reduce thermalization losses, increase the lifetime of the solar cell, and leads to relatively higher PV conversion efficiency in tandem or multijunction solar cells as compared to single junction cells.[14] Splitting and exploiting incident light spectrum using tandem or multijunction solar

S. K. Chamoli, S. Singh, W. Li
GPL Photonics Laboratory
State Key Laboratory of Applied Optics
Changchun Institute of Optics
Fine Mechanics and Physics
Chinese Academy of Sciences
Changchun 130033, China
E-mail: ssingh49@ur.rochester.edu; weili1@ciomp.ac.cn
S. K. Chamoli, W. Li
University of Chinese Academy of Science
Beijing 100039, China
S. Singh, C. Guo
The Institute of Optics
University of Rochester
Rochester, NY 14627, USA
E-mail: guo@optica.rochester.edu
The ORCID identification number(s) for the author(s) of this article can be found under https://doi.org/10.1002/adts.202200632

DOI: 10.1002/adts.202200632

cell, spectral splitting inside the cell, is more practical than using grating-like optical elements or filters to split the solar spectrum into different cells.[15–17]

Recently, silicon/perovskite tandem solar cells are investigated to surpass the single-cell QS limit.[3] The adopted approach stabilizes the perovskite material and leads to a record efficiency of 29.15%.[3,18–21] Despite the competitive photovoltaic efficiency, a major challenge is the poor material stability, which remains an obstacle in the development of commercially viable $CH_3NH_3PbI_3$ solar cells.[22–24] Therefore, perovskite crystal growth, solar cell fabrication, and their testing all need to be performed in a controlled environment in a glove box. In order to facilitate scientific progress toward commercial applications, PSC degradation mechanisms have been studied under vacuum and in nitrogen atmospheres to investigate their microscopic and macroscopical behavior.[25] However, PSCs need to operate in ambient outdoor conditions, therefore, their performance testing in a controlled environment is not practical. To address stability and degradation issues, commercial PSCs are vacuum encapsulated between transparent and environment-proof sheets. A recent study examined grain surface passivation as a solution to stability issues in all-perovskites tandem solar cells.[26] It has been shown that crystalline silicon and perovskites are a good match, particularly $CH_3NH_3PbI_3$, the best-studied material out of the group of perovskites, which has a band gap of ≈1.6 eV. The energy conversion efficiency of a tandem solar cell can be maximized with a combination of top and bottom panels with matching bandgaps. Two-terminal tandem solar cells can reach energy conversion efficiencies equivalent to four-terminal tandem solar cells if the bandgaps of the top and bottom solar cells are matched and the short-circuit current of the two-terminal tandem solar cells is matched.[27] For the top cell to be the most efficient, the bandgap must be equal to $E_{G\_top} = 0.5 \times E_{G\_bottom} + 1.5$ eV.[27] The relationship is valid if the bandgap of the bottom cell stays in a range from 0.85 to 1.2 eV. Hence a variety of material combinations can be selected. Crystalline silicon with a bandgap of 1.15 eV is well suited as a bottom solar cell. Hence, a lot of research has been devoted to the development of tandem solar cells using a crystalline silicon bottom solar cell.[27] For this combination, the highest energy conversion efficiency could be achieved if the bandgap of the top cell material is equal to ≈1.7 eV. So, for tandem solar cells with crystalline silicon as bottom cells, the energy conversion efficiency is maximized when the bandgap of the top diode is 1.725 eV. The maximum conversion efficiency of 43% is achieved using the perovskite ($MAPbI_3$) absorber with a bandgap of 1.6 eV.[27] Additionally, few studies have focused on tandem solutions of all perovskites.[28] Several studies have addressed perovskite solar cells' electronic[29–32] and optical properties[33–35] for the purpose of understanding and optimizing conversion efficiency and photon management in the perovskite solar cell.[36,37] A high extinction coefficient and a large diffusion length of perovskite make them suitable materials for solar cells with a large short-circuit current density and high energy conversion efficiency.[38–40] Thin-film solar cells enable an efficient charge carrier collection with fewer constraints on diffusion lengths.[41,42] Due to shorter path lengths, these cells offer low conversion efficiency. Adding an efficient light-trapping cavity to a thin-film solar cell could lead to large power conversion efficiency.[10,27,43] Nanostructured solar cells are nevertheless concerned about surface recombination losses caused by the increased surface area of the nanostructured cells.[44] Generally, a planner arrangement is used in conventional tandem solar cells resulting in the escape of light after a few oscillations.[27] Designing an efficient cavity that can trap light for many oscillations in tandem solar cells to enhance their efficiencies remains underexplored.

In this work, we introduce a novel wedge-shaped tandem solar cell that acts as a light-trapping element. The designed wedge cell significantly reduces the cell thickness, and thus, material requirement, and achieves 17.18% higher conversion efficiency over a planner cell of the same thickness of ≈2 μm. The cell consists of two active layers in a wedge fashion: a wide bandgap $CH_3NH_3PbI_3$ as the upper cell and a narrow bandgap Si as the bottom cell. Due to the wedge shape of the bottom cell, the normally incident light gets refracted and trapped into the cell leading to multiple bounces before leaving the cell. Optical and electrical simulations are performed to analyze, characterize, and compare the performances of the wedge tandem cell with a conventional planar tandem cell of the same thickness. It is interesting to note that the wedge tandem cells absorb up to 10% larger solar power than flat tandem cells of the same thickness. The wedge tandem cells have a stronger light-trapping effect in a longer wavelength region of the solar spectrum. The geometry of the wedge tandem cell is optimized to maximize its performance. Additionally, we numerically characterize the *I–V* and *P–V* curves of the wedge and planner tandem cells with considering fundamental loss mechanisms. For simplicity, we used a four-terminal (4T) tandem cell configuration where the upper and lower cells are electrically independent but optically connected in series.[45] In this configuration, current matching between sub-cells is not required. Therefore, the efficiency of 4T-configuration tandem cells has far less dependency on the bandgap of the top cell material over similar two-terminal (2T) cells. In our 4T-tandem cell design, the perovskite top cell is placed on top of the silicon bottom cell with an air gap in between. Many designs and methods have been proposed such as the Bragg reflector,[46] photonics crystal,[47,48] nanoscale back contacts,[49] and a stack of perovskite and bifacial c-Si solar cells.[50] The wedge geometry provides a better charge collection efficiency and a lower recombination rate over the corresponding planner cell. One of the possible advantages of the proposed wedge cavity tandem cell is better spectral management to overcome the tradeoff in a nanostructure-based light-trapping system.[51] The wedge-shaped tandem cells can be fabricated with ease using an optimized electrospray (ES) deposition process[52] or glancing angle deposition,[53,54] with a certain deposition rate. Translating the substrate in the 2D plane would enable large surface area deposition for the proposed wedge-shaped solar panel. Other applications, such as polarization switches and linear color variable filters, can also benefit from our design.

2. Proposed Design and Methods

Schematics of the proposed wedge cavity tandem solar cell and a typical planar tandem cell are shown in **Figure 1**. The cell consists of an infinite number of wedges and planar arrays (unit cell) as shown in the zoomed portion of the schematic. The top contact layer is made of a transparent conducting oxide (TCO),

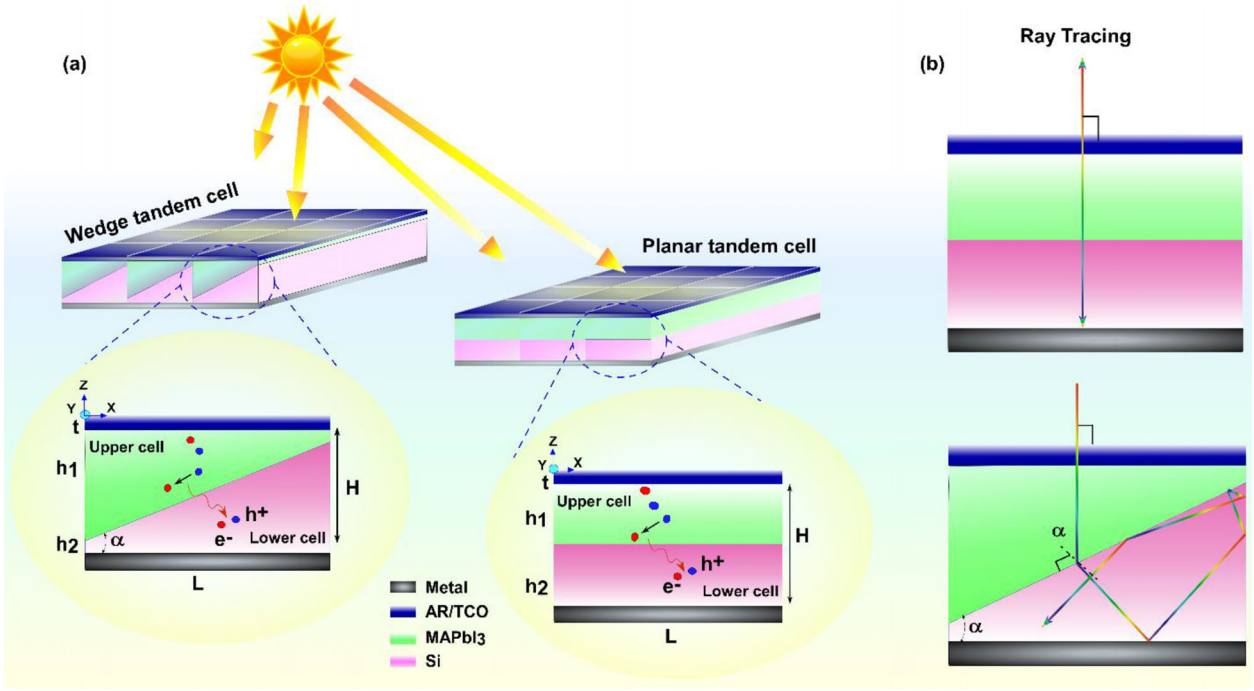

Figure 1. a) Schematics of the proposed wedge tandem cell and a planar tandem cell. The cell is an array of unit cells shown in the zoomed view. $MAPbI_3$ and Si are the active materials for the upper and lower cells, respectively. *L* is the length of the unit cell and *H* is the total cell thickness. The top layer is a transparent conducting oxide (TCO)/anti-reflection (AR) coating such as ITO or FTO. In the case of the wedge cell: α is the angle that decides the role of the upper and lower cells, for example, $\alpha = 45°$ (i.e., $L = H$) represents an equal contribution of the upper and lower wedge cells. b) Planar and wedge type cells ray tracing cartoon. In wedge cells, light experiences multiple bounces before leaving the cell, resulting in an increase in absorption, which is illustrated in detail in Figure S2, Supporting Information, with the aid of ray tracing simulations.

which also helps to reduce the reflection losses. A typical example is ZnO, which exhibits a comparable refractive index to the perovskite layer, indicating that light is not reflected from the ZnO/perovskite interface. The upper cell is made of $MAPbI_3$ perovskite and the bottom cell is made of crystalline Si. The total thickness ($H = h_1 + h_2$) of the unit cell is the same for the wedge and planar tandem cells. *L* is the length of a single-unit cell. Aluminum due to its high reflection in the visible and near IR and low-cost material is chosen as a bottom reflector or metallic contact.[55,56] An experimental consideration would be the intermediate layer substrate and the crystalline Si, for example, using amorphous Si.[57,58] α is the wedge angle and a defining parameter that needs to be optimized to understand the contributions from the upper and lower wedge cell. An illustration of the effectiveness of a wedge cavity in terms of the index as a function of transverse direction can be found in Figure S1, Supporting Information. A feature like this can be useful in applications such as linear color variable filters.[53] We used a finite difference time domain (FDTD) simulation to investigate the optical properties of the tandem solar cells. FDTD is accepted as a very effective strategy to systematically simulate the photoelectric performance of SCs.[59–61] With FDTD simulation, we optimized the thickness and compared the absorption of the wedge and planar cells. Considering plane wave propagating in the *z*-direction with wavelength ranging from 400 to 1200 nm that covers the majority of AM 1.5G solar spectrum (**Figure 2**a). A perfectly matched layer (PML) is used in the *z*-direction while periodic boundary conditions are chosen in the *x*–*y* directions. Refractive index data for $MAPbI_3$ and Si are taken from the following references and extrapolated till 1200 nm.[62,63] The FDTD solver calculates the electric field profiles by solving Maxwell's equations and then the obtained electric field is used to calculate the optical power absorbed per unit volume in the cell using $P_{abs} = -0.5\ \omega|E|^2 Im(\varepsilon)$, where ω, $|E|^2$, and $Im(\varepsilon)$ are the angular frequency, electric field intensity, and imaginary part of the permittivity, respectively. After calculating P_{abs}, J_{SC} that corresponds to the integrated photon flux of the AM 1.5G with the respective absorbance can be calculated as follows: $J_{SC} = e \int_{\lambda_1}^{\lambda_2} \emptyset_{AM1.5G}(\lambda)\ P_{abs}(\lambda)\ d\lambda$, where $\emptyset_{AM1.5G}(\lambda)$ is the incident photon flux and *e* is the elementary electron charge. Ray tracing cartoon in the case of wedge versus planar cell is shown in Figure 1b, in planar cell light just reflects back, however, in wedge geometry, light is refracted into the bottom cell due to the incident angle coming from wedge angle. In Figure S2, Supporting Information, the light-trapping effect in the wedge cell is shown with the help of ray tracing simulation at different locations of the cell and compared with the planar cell. It is evident that light gets bounced multiple times before leaving wedge cells and this results in increased absorption.

3. Results and Discussion

3.1. Optical Simulations

Figure 2a shows spectral irradiance at global air mass 1.5 (AM1.5G), showing a major contribution from the sun in the

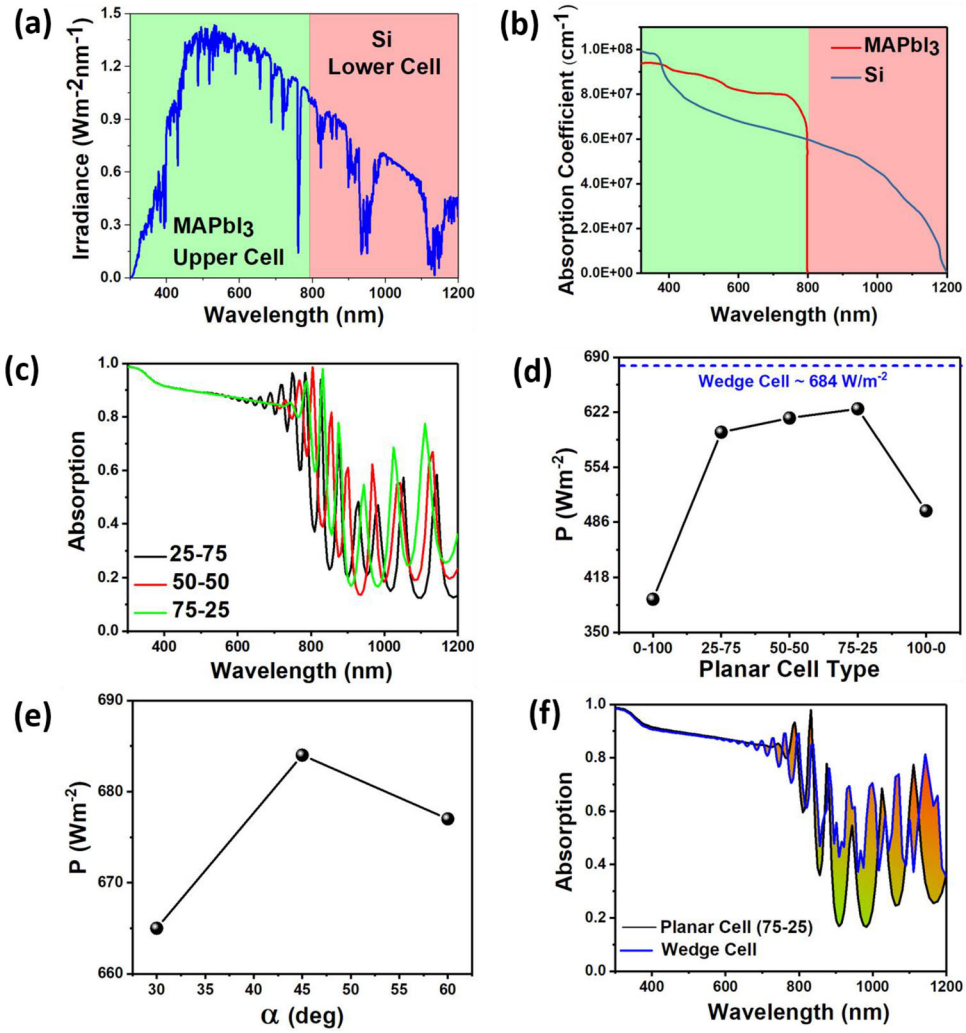

Figure 2. Optimization for the wedge and planar tandem cell. a) The spectral irradiance at global air mass 1.5 (AM1.5G), showing a major contribution in the range of 400 to 1200 nm, b) absorption coefficient of crystalline silicon and $MAPBI_3$, c) absorption spectra from $H = 2$ μm thick planar tandem cell for different thickness combinations of $MAPbI_3$ (the upper cell) and Si (the bottom cell): 25–75 corresponds to 500 nm $MAPbI_3$ and 1500 nm Si, 50–50 corresponds to 1000 nm $MAPbI_3$ and 1000 nm Si, 75–25 corresponds to 1500 nm $MAPbI_3$ and 500 nm Si, d) Power absorbed by different planar tandem cells and the wedge cell with $\alpha = 45°$ and $H = 2$ μm ($h_1 = 1800$ nm and $h_2 = 200$ nm, blue horizontal dotted line), e) power absorbed by a wedge tandem cell as a function of wedge angle α, and f) absorption spectra from the wedge cell with $\alpha = 45°$ and the planar cell 75–25 with the same total thickness of 2 μm.

range of 400 to 1200 nm. $MAPbI_3$ has a high optical absorption coefficient and a low penetration depth. Opposite to this, crystalline Si has comparatively a lower absorption coefficient and a higher penetration depth as depicted in Figure 2b. In addition, $MAPbI_3$ has a diffusion length that is greater than its penetration depth. Thus, light trapping is not necessary for increasing solar cell short-circuit currents or quantum efficiency. As Si is an indirect semiconductor, its penetration depth is greater than the thickness of most solar cells. This is why light trapping is applied to increase short-circuit efficiency. We begin our study by calculating optical absorption from the wedge and planar tandem cells for a fixed value of $H = 2$ μm. Noticeably, the thicknesses of the wedge and planar geometries can have any value, however, we are interested in comparing the absorption of the wedge and planar cells for the same thickness, and if it is less thick, it is computationally easy to calculate. In the case of the planar tandem cell, there are various possible combinations for h_1 and h_2. Therefore, to figure out the best combination of h_1 and h_2 for maximum absorption, we vary h_1 from 0 nm (0%, i.e., no contribution from the upper cell) to 2 μm (100%, i.e., the only upper cell is contributing) simultaneously h_2 from 2 μm (100%, i.e., only lower cell is contributing) to 0 nm (0%, i.e., no contribution from lower cell). Among all, the following three combinations are chosen and corresponding absorption spectra are simulated: i) 500 nm $MAPbI_3$ and 1500 nm Si (25%: the upper cell and 75%: the lower cell), ii) 1500 nm $MAPbI_3$ and 500 nm Si (75%: the upper-cell and 25%: the lower-cell), and iii) 1000 nm $MAPbI_3$ and 1000 nm Si (50%: the upper-cell and 50%: the lower-cell). The absorption spectrum (Figure 2c) exhibits multiple absorption peaks in the interference (IF) region and effectively contributes to enhanced absorption. One can observe that in all three cases, the absorption peaks are shifting in the interference region with almost the same absorp-

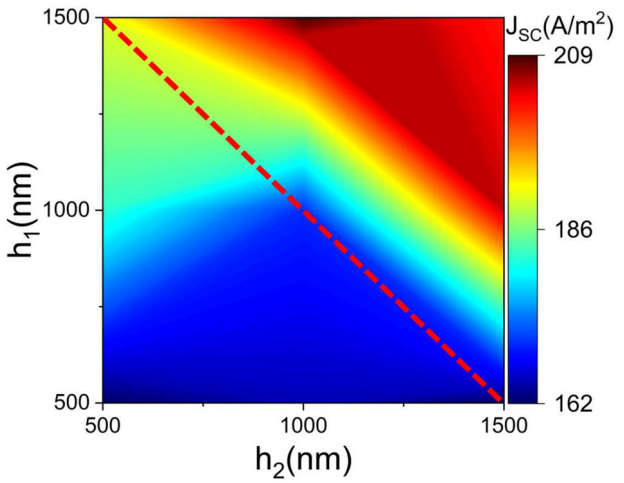

Figure 3. J_{SC} as a function of h_1 and h_2 for planar tandem cells. The red dotted line represents the region below which total thickness $h_1 + h_2 = 2$ μm, the thickness we are interested in our calculations.

tion in the Beer–Lambert (BL) region. However, the bandwidth of the absorption peaks is narrow, but these narrow peaks have significant contributions to the overall optical response and ultimately enhance the performance of the cell. The wedge and planar Si layers are also compared in Figure S3, Supporting Information, and the absorption results show a significant difference. To figure out the best combination, we calculated the power absorbed by the cell using: $P = \int_{\lambda_1}^{\lambda_2} I_{AM1.5G}(\lambda) \times Absorption(\lambda)\, d\lambda$ as shown in Figure 2d. It is evident that the power absorbed is maximum for 75–25 combination, where $MAPbI_3$: the upper and Si: the bottom cells are 1500 and 500 nm thick, respectively. Similarly, we optimize the wedge cell to pick the best wedge angle, α, as shown in Figure 2e. The maximum absorption occurs at $\alpha = 45° \approx 684\ W\ m^{-2}$. Figure 2f shows absorption spectra for the optimized planar cell (75–25) and a wedge tandem cell with the same total thickness ($H = 2$ μm) and the wedge angle $\alpha = 45°$. One can see a significantly larger absorption in the wedge-shaped tandem cell over the planer cell due to relatively better light trapping. Consequently, the power absorbed by the wedge cell is ≈10% larger than the best planar cavity (see blue dotted line in Figure 2d) of the same total thickness.

Furthermore, we plotted the J_{SC} value as a function of h_1 and h_2 to optimize the total thickness and thicknesses of individual sub-cells (**Figure 3**). In this figure, the maximum value for the total cell thickness $h_1 + h_2$ is 2.5 μm ($h_1 = 1.5$ μm and $h_2 = 1$ μm). However, for our purpose, the red dashed line represents the J_{SC} regions corresponding to total thickness <2 μm. The maximum J_{SC} value occurs when h_1 is 1.5 μm and h_2 is 0.5 μm for a 2 μm thick planar tandem cell.

The physical mechanism behind the light trapping is as follows: a normally incident light at top of the upper cell is off-normal at the top of the lower cell and incident at an angle α (the wedge angle). That means, for normal incident light at the top of the upper cell, the angle of incidence at the lower cell is determined by α (see Figure 1a). Following Snell's law, the light enters at an angle into the bottom cell and gets trapped inside. Here, the bottom cell acts as a refractive element. The trapping effect can be directly visualized by observing the electric field distribution in the cell. **Figure 4** shows the electric field profile for a wedge (a,c) and planar (b,d) tandem cell. Two distinct regions are evident: i) the Beer–Lambert (BL) region and ii) the wave IF region. The BL region appears at a low wavelength range where the light gets absorbed rapidly by the cell and no light bounces back from the bottom metal reflector (see Figure 4a,b). However, due to wedge geometry near the extreme right corner of the wedge cell, the light penetrates the upper cell and bounces back from the bottom metallic layer. Therefore, in the wedge tandem cells, even at low wavelength regions, both the upper and lower cells are involved in the light-harvesting, while in the planner tandem cell, only the upper cell is the photon harvester. The enhanced light harvesting can certainly help to improve the existing trade-off in the tandem cell.[51] On the other hand, at a higher wavelength region (the IF region), the planar tandem cell simply shows interference between the incident light and the light reflected from the metallic layer (see Figure 4d). Unlike the planer cell, the light incidents at the top of the lower cell at an angle and gets refracted and bounces multiple rounds before escaping from the cavity resulting in a significantly increased optical path or light trapping (see Figure 4c). The efficient light trapping in the wedge cell is the reason behind the enhancement in the absorption and can be utilized to enhance photon harvesting or cell performance. Similarly, Figure S2, Supporting Information, provides a ray diagram showing light trapping.

Generally, optical absorbance and available solar flux both decreases with an increase in the zenith angles, therefore, regular solar cells have lower efficiency during morning and evening hours. For efficient solar energy harvesting, angular insensitivity in optical absorption is highly desirable in solar cells to operate efficiently even when the sun is at larger zenith angles. For this purpose, an omnidirectional anti-reflective coating is required in solar cells.[64,65] Additionally, solar flux available at a horizontally lying solar cell can be calculated using $I = I_0 \cos\theta$; where I_0 is 1000 W m^{-2} and θ is the solar zenith angle. **Figure 5**a shows variation in the available solar flux at a horizontally lying solar panel with the zenith angle. Figures 5b and 5c demonstrate spectral absorption as a function of incident angle for the wedge and planar tandem cells, respectively. Both types of tandem cells show nearly omnidirectional characteristics for incidence angle in the shorter (400–800 nm) wavelength region. However, at a longer wavelength region (from 800 to 1200 nm), the wedge cell has larger absorption than that of the planar tandem cell. This is simply due to the enhanced trapping effect in wedge cells that leads to enhancement in optical absorption. Furthermore, we calculate the average absorption of both cells as a function of the incident angle in Figure 5d. From this, it is evident that the absorption of the wedge cell is always higher than that of the plane cell at all angles. Average absorption $\bar{\alpha}$ is calculated using following expression at each angle[66]

$$\bar{\alpha} = \frac{\int_{0.4\mu m}^{1.2\mu m} \alpha(\lambda) \times I_{AM1.5}(\lambda)\, d\lambda}{\int_{0.4\mu m}^{1.2\mu m} I_{AM1.5}(\lambda)\, d\lambda} \quad (1)$$

where $I_{AM1.5}(\lambda)$ and $I_{BB}(\lambda)$ are solar irradiance and blackbody spectrum at a given wavelength and temperature.

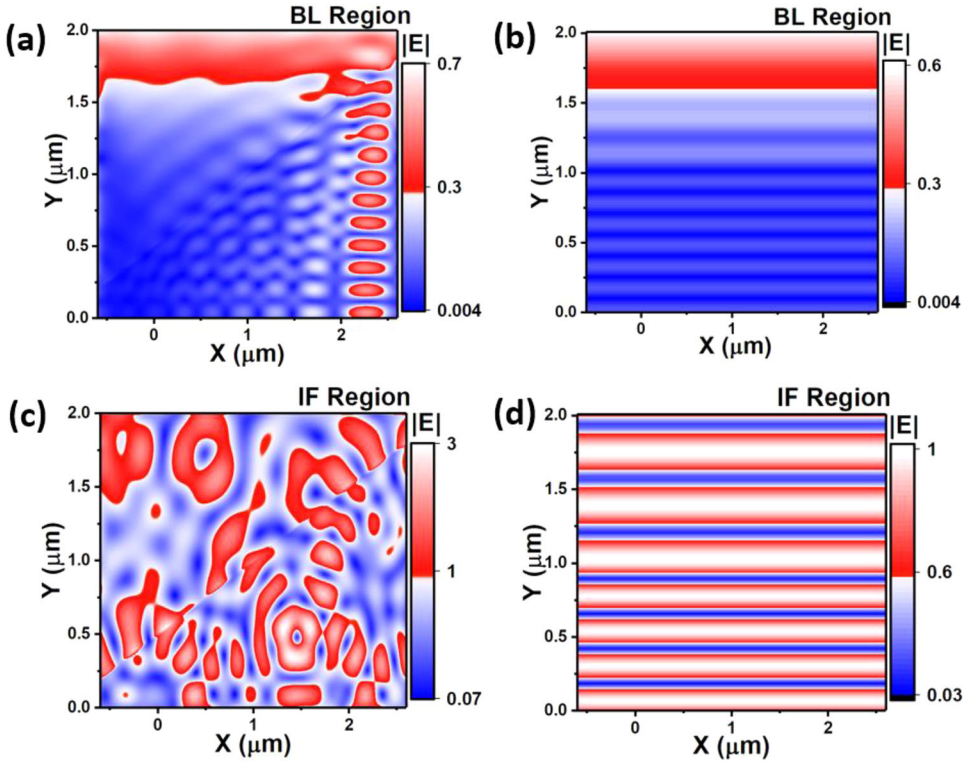

Figure 4. Electric field distribution and trapping effect. Electric field intensity distribution at a shorter (BL region) and higher (interference region) wavelength for a,c) wedges and b,d) planar cells. Light-trapping effect for wedge cavity at higher wavelengths are visible, where normally incident light is trapped into the cavity. On the shorter wavelength side material itself has high absorption and light gets absorbed within a few hundred nanometers following Beer–Lambert's (BL) law. The incident light of 400 nm is absorbed completely by the top perovskite cell. At 750 nm, however, a small fraction of the light enters the bottom cell. For an incident light of 1000 nm, nearly all of the light is transmitted in the bottom cell, where it is absorbed.

Further, on the basis of the absorption data in Figure 4d, we calculated J_{SC} as a function of the incident angle for both cells in **Figure 6**. Due to a higher optical absorption, the wedge cell has a higher J_{SC} value at all incident angles. In Figure S4, Supporting Information, we discuss in detail the optical spacer layer (OSL) of a 4T configuration.[60] We plotted the average absorption from tandem cells as a function of the index of OSL and thickness at higher wavelengths. Due to the fact that long-wavelength light can pass the top cell and mostly contribute to photogeneration in the bottom cell.

3.2. Electrical Simulations

The basic structure of a solar cell is a *p–n* or *p–i–n* junction, which converts sunlight into electricity.[67,68] Photons are first absorbed, resulting in electron/hole pairs. The photogenerated electron/hole pairs are separated in a second step and then collected. The photogenerated charge is collected to the contacts of the solar cell by diffusion, drift, or a combination of both. We used COMSOL Multiphysics simulations to solve the Poisson and continuity equations for the carrier dynamics, and finally, we compared the current–voltage characteristic ($J-V$) of the planar and wedge tandem cells. The cell thickness $H = 2$ μm and area = 4 μm^2 are the same for both tandem cells. We used user-defined functions for photocarrier generation and photocarrier recombination rates for the upper and lower cells independently. The coupling between the optical (photocarrier generation rate) and electrical simulations is governed by the following set of equations

$$\nabla \times \left(\varepsilon_s \nabla \Psi\right) = -\rho \tag{2}$$

$$\frac{\partial n}{\partial t} = \frac{1}{q}\left(\nabla \times J_n\right) - U_n + G_n \tag{3}$$

$$\frac{\partial p}{\partial t} = \frac{1}{q}\left(\nabla \times J_p\right) - U_p + G_p \tag{4}$$

where Ψ is electrostatic potential, n and p are electron and hole concentrations, ε_s is the material permittivity, U_n and U_p are recombination rates for electrons and holes, respectively, and G_n and G_p are photogeneration rates of electrons and holes, respectively. Recombination can generate or lose charge carriers based on a variety of physical properties depending on the material properties, external conditions, and energy states (defects) within the band gap. With several built-in and user-defined options for recombination mechanisms, COMSOL's Semiconductor Module allows capturing the exchange and loss of charge carriers through recombination. As c-Si cells undergo Auger recombination at higher carrier density, SRH recombination is also assumed, though unlike Auger recombination and radiative recombination, it is theoretically possible to eliminate SRH recom-

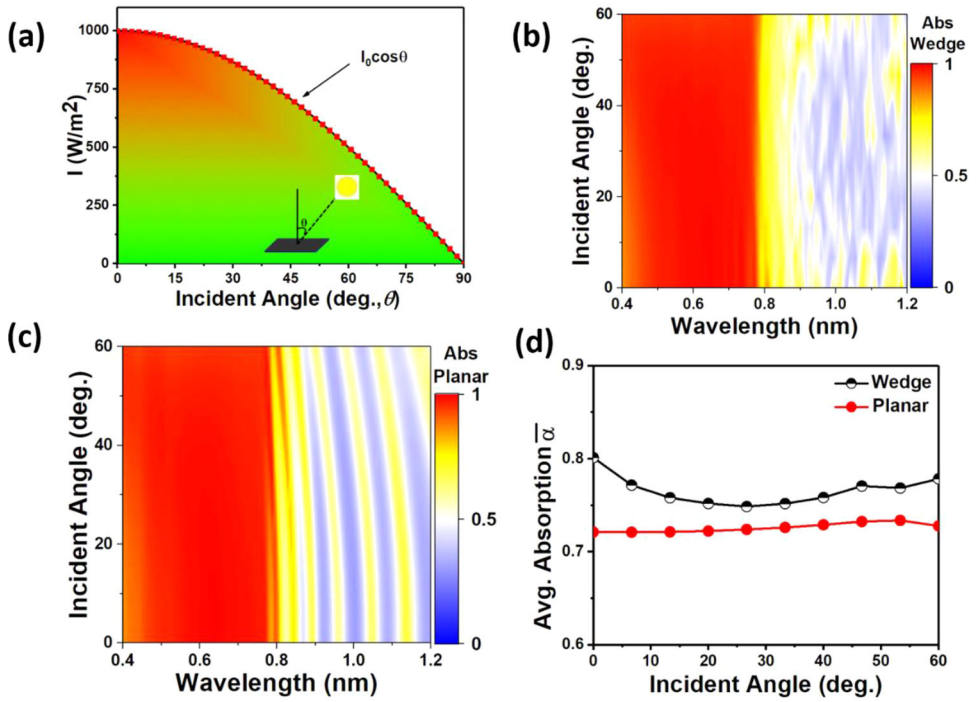

Figure 5. a) Angular analysis. Intensity absorbed by the PV module as a function of incident angle (θ) between solar cell and source. Absorption as a function of incident angle and wavelength in case of b) planar tandem cell and c) wedge tandem cell. d) Angular dependence of average absorption $\bar{\alpha}$ on incident angle θ for planar and wedge cells. All these results were obtained from the wedge cell with $\alpha = 45°$ and 75–25 planar cell combination.

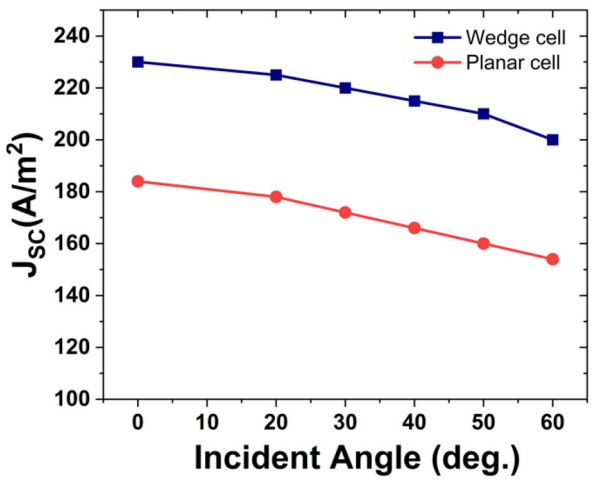

Figure 6. J_{SC} as a function of incident angle for wedge and planar tandem cell.

Table 1. Electrical parameters used in the model for Si and perovskites.

Parameter	Si	$CH_3NH_3PbI_3$
Dielectric constant	11.7	13
Bandgap [eV]	1.1	1.55
Electron affinity [eV]	4.05	3.6
Electron and hole mobility [$cm^2\ V^{-1}\ S^{-1}$]	1450, 500	50, 50
SRH lifetime [μs]	10	8
Effective density of states in conduction band ($1\ cm^{-3}$)	2.54×10^{19}	3.64×10^{19}
Effective density of states in valence band ($1\ cm^{-3}$)	1.04×10^{19}	1.36×10^{18}
Auger recombination factor, electrons [$cm^{-6}\ s^{-1}$]	2.8×10^{-31}	2.7×10^{-29}
Auger recombination factor, holes [$cm^{-6}\ s^{-1}$]	9.9×10^{-32}	4.6×10^{-29}

bination by eliminating defects[69,70] and the most dominating loss mechanism in the solar cells.[71] In our model, The SRH (U_n & U_p) and Auger recombination R_{Aug} are implemented as follows

$$U_n = U_p \propto N_t \left(pn - n_0 p_0\right) \tag{5}$$

$$R_{Aug}\left(V\right) = \left(C_n + C_p\right) W n_i^3 \exp\left(3qV/2KT\right) \tag{6}$$

where C_n & C_p are conduction-band (valence-band) Auger coefficients (see **Table 1**). Assuming that each absorbed photon generates one electron–hole pair, the total photogeneration rate for electron and holes are given by the following integral

$$G_n = G_p = \int_{300\ nm}^{1200\ nm} \frac{\pi}{h} \varepsilon'' E^2\left(x, y, z, \lambda\right) d\lambda \tag{7}$$

where ε'' is an imaginary part of dielectric permittivity and $E^2(x, y, z, \lambda)$ is the electric field distribution in each layer at a

given incident wavelength by solving the Helmholtz equation. The charge density ρ is given by

$$\rho = q\left(n - p + N_A - N_D\right) \tag{8}$$

N_A and N_D are the total number of positive and negative charges in the model including dopants or impurities, respectively. Electron and hole current densities are given by the following expressions including drift and diffusion part

$$J_n = -q\mu_n n\nabla\Psi + qD_n\nabla n \tag{9}$$

$$J_p = -q\mu_p p\nabla\Psi + qD_p\nabla p \tag{10}$$

where μ_n and μ_p are electron and hole mobilities, respectively, while D_n and D_p are the electron and hole diffusion coefficients, respectively. Finally, the total current density J is the sum of Equations (6) and (7), that is, $J = J_n + J_p$. The top and bottom contact layers have a peak electron density of 10^{19} cm^{-3} and have a Gaussian drop-off in the z-direction. The bulk of the cell is doped with constant n doping of 10^{16} cm^{-3}. As shown in Figure S5, Supporting Information, there is a PN junction region in both the top and bottom cells of the tandem cell. Depending on which type of metal contacts are being considered, boundary conditions (BC) affects the currents. When Schottky contacts are present, BC depends on carrier concentrations at metal/semiconductor interfaces and recombination speeds, S_n or S_p

$$J_n \times \hat{n} = -qS_n\left(n - n_0\right) \tag{11}$$

$$J_p \times \hat{n} = -qS_p\left(p - p_0\right) \tag{12}$$

In this equation, $\hat{n}$ is the unit normal at the boundary and n_0 and p_0 are the concentrations of electrons and holes at equilibrium. However, in our model surface recombination is not taken into account.

A description of the open-circuit voltage and fill factor of the solar cells is necessary to provide a realistic prediction of their energy conversion efficiency. Figures 5c and 5d exhibit the J–V and – V curves for the wedge and planar tandem cells, respectively. These curves are generally used to extract the important PV characteristics of a cell. A solar cell's energy conversion efficiency is a parameter that characterizes its performance, which is measured by the ratio of the electrical output power density to the optical input power density. The electrical output power density of the solar cell is determined by $V_{mp} \times J_{mp}$, where V_{mp} and J_{mp} are the voltage and current density, respectively, at maximum power. The values for V_{mp} and J_{mp} are obtained from the cell's J–V characteristic. The short-circuit current density, fill factor, and open-circuit voltage parameters are introduced in order to correlate the J–V characteristics with solar cell physics. Short-circuit current density is provided by $J(V = 0) = J_{SC}$, whereas $J(V = V_{OC}) = 0$ is the open-circuit voltage.

$$\eta = \frac{V_{mp} \times J_{mp}}{P_{in}} = \frac{V_{OC} \times J_{SC} \times FF}{P_{in}} \tag{13}$$

The fill factor can be calculated as follows using Equation (14)

$$FF = \frac{V_{mp} \times J_{mp}}{V_{OC} \times J_{SC}} \tag{14}$$

The simulation parameters are the same for both (planar and wedge) tandem cells and are given in Table 1.

Thin-film tandem cells are available in two configurations: monolithically integrated two-terminal (2T) architecture and mechanically stacked four-terminal (4T) setup. Thin-film tandem cells can either be integrated monolithically into a two-terminal architecture or mechanically stacked into a four-terminal array. In the 2T structure, top and bottom sub-cells are electrically coupled, whereas, in the 4T structure, two sub-cells are optically coupled, but electrically independent of one another. 2T architecture has a series of electrical coupling between two sub-cells, requiring each sub-cell's current to be the same. This constrains material selection in this 2T design.[50] A mechanically stacked 4T device, on the other hand, is not limited by current matching issues. Each device is fabricated separately and then electrically connected either in series or parallel through an external circuit.[72,73] COMSOL Multiphysics can be used to simulate either configuration with the proposed wedge geometry by following the equations described above. In our calculation, we used the 4 T configuration of tandem cells for simplification of the simulations. In **Figures 7**a and 7b, we show the typically used 4T configuration for wedge and planar tandem solar cells, respectively. After absorption of incident photons, electron–hole pairs are generated at the top and bottom electrodes and collected. In Figure 7c, the general considerations related to tandem cells are shown, that is, low photon absorption in the top cell and high photon absorption in the bottom cell. The non-normal angle of the light incident in the wedge causes light to be trapped inside the bottom cell, resulting in higher absorption than a planar wedge. Wedge cell increase electron–hole pairs by improving absorption in the bottom cell. Thus, the wedge tandem cell results in higher J_{SC} and output power than planar cells, respectively. Figures 7d and 7e illustrate the current density and voltage (J–V) curves for planar and wedge cells, respectively. We summarize and compare the parameters J_{SC}, V_{OC}, FF, P_{MP}, and η of the wedge and planner tandem cell for the top and bottom cells in **Table 2**. Light absorption in the top cell decreases the J_{SC}, V_{OC}, FF, and P_{MP} parameters in the bottom cell. P_{MP}'s of both top and bottom cells should be considered when calculating the efficiency of the 4T tandem structure. It is expected that power output in the bottom cell of the wedge and planar cells will differ depending on absorption levels, while in the top cell, power output will be comparable. This difference in power output can be attributed to light trapping in the wedge cell. It appears that wedge cells (≈17.4%) have higher efficiency than the planar tandem cell. The calculated J_{SC} is comparable to previously reported experimental values.[27,74] Short-circuit currents are generally caused by low recombination or high generation rates, short diffusion lengths, and band offset between layers in the solar cell (between active medium and electron and hole transport layers).[75]

In order to further understand the reasons for higher J_{SC} and better performance in wedge geometry compared to planar geometry, recombination rate calculations are performed (Figure S6, Supporting Information). In the case of planar tandem cells,

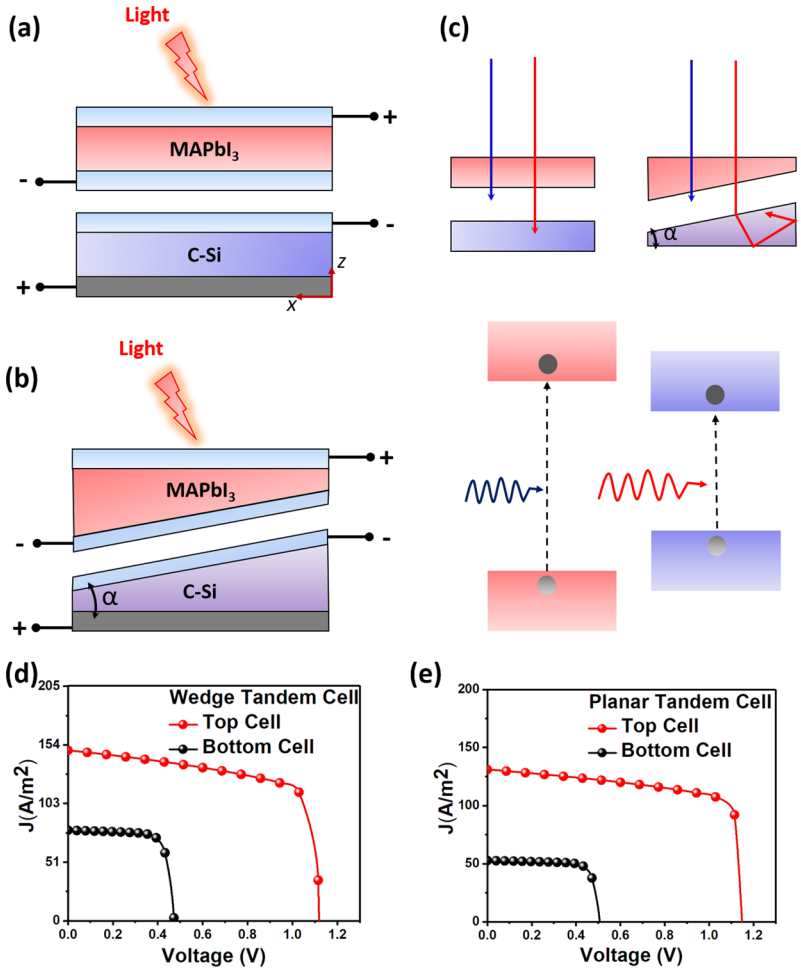

Figure 7. Current density (*J*)–voltage (*V*) characteristics, *J*–*V* analysis. Standard 4T configuration for tandem cell for a) conventional planar and b) wedge tandem cell. c) Diagram showing light absorption in planar and wedge tandem cells. As shown in the cartoon at the top, low-wavelength photons are absorbed by the top cell, while high-wavelength photons are absorbed by the bottom cell. The bottom cell in a wedge tandem cell shows light trapping as shown in the upper cartoon. Current–voltage (*J*–*V*) and power voltage (*P*–*V*) curve of d) wedge cell for wedge angle 45° and e) planar cell for 75–50%. For both top and bottom wedge cells, $h_1 = 1500$ nm and $h_2 = 500$ nm.

Table 2. *P*–*V* characteristics for wedge and planar cell.

P–*V* parameters	Planar tandem cell		Wedge tandem cell	
	Top cell	Bottom cell	Top cell	Bottom cell
J_{SC} [A m^{-2}]	131	53	150	80
V_{OC} [V]	1.14	0.5	1.11	0.47
FF	0.73	0.76	0.72	0.75
P_{MP} [W m^{-2}]	110	18	115	35
η [%]	12.8		15.0	

the band diagram is the same at all locations, so all the photo-generated electron–hole pairs have to travel the same distance to contribute to current and voltage. However, in the case of wedge geometry, obviously, the band bending is different at different locations. So, the generated photo-generated electron–hole pairs due to near proximity at 1 and 3 can be extracted by electrode fast without being recombined. Location 2 is somewhat similar to the planar case in wedge geometry. As a result, wedge cell has a better collection efficiency than planar cells. Compared to a planar geometry, the wedge geometry exhibits a lower rate of recombination resulting in an increased J_{SC}.

4. Conclusions

In summary, we designed a novel wedge tandem cell that acts as an efficient light-trapping element and compares its *P*–*V* characteristics with a typically used planar tandem cell using opto-electrical analysis. We optimized and compared both tandem cells using optical and electrical simulations and found that wedge tandem cells with a 45°-wedge angle were more efficient than planar cells. The wedge cell showed a 30% higher optical absorption in the near-infrared region when compared to a planar tandem cell resulting in a 10% increase in power absorption. Based on electric field simulations, this is attributed to the optical light-trapping effect that results in an increase in the optical path

length and finally its absorption. We calculated and compared the I–V and P–V characteristics of both cells, estimating 150 W m^{-2} for the wedge cell and 128 W m^{-2} for the planar tandem cell in terms of maximum output power. Finally, we compared wedge with planar tandem cells based on energy band diagrams and recombination rates. Wedge geometry has a better charge collection efficiency and a lower recombination rate. Overall, the wedge cell performs better optically and electrically than the planar cell. The proposed light-trapping scheme can be fabricated with ease using methods such as glancing angle deposition and direct electrospray deposition.

Supporting Information

Supporting Information is available from the Wiley Online Library or from the author.

Acknowledgements

This work was supported by the National Natural Science Foundation of China (grant nos. 62134009 and 62121005), the Innovation Grant of Changchun Institute of Optics, Fine Mechanics and Physics (CIOMP), Jilin Provincial Science and Technology Development Project (grant no. YDZJ202102CXJD002), Development Program of the Science and Technology of Jilin Province (20200802001GH). S.K.C. acknowledges his sponsorship by "CAS-TWAS Presidential Fellowship for international doctorate students."

Conflict of Interest

The authors declare no conflict of interest.

Data Availability Statement

The data that support the findings of this study are available on request from the corresponding author. The data are not publicly available due to privacy or ethical restrictions.

Keywords

light trapping scheme, tandem solar cell

Received: September 2, 2022
Revised: November 9, 2022
Published online: November 27, 2022

[1] N. S. Lewis, D. G. Nocera, *Proc. Natl. Acad. Sci. USA* **2006**, *103*, 15729.
[2] P. IEA. Renewables 2019, IEA, IEA (2019), Renewables 2019, https://www.iea.org/reports/renewables-2019 (accessed: October 2019).
[3] Z. Fang, Q. Zeng, C. Zuo, L. Zhang, H. Xiao, M. Cheng, F. Hao, Q. Bao, L. Zhang, Y. Yuan, W. Q. Wu, D. Zhao, Y. Cheng, H. Tan, Z. Xiao, S. Yang, F. Liu, Z. Jin, J. Yan, L. Ding, *Sci. Bull.* **2021**, *66*, 621.
[4] W. Shockley, H. J. Queisser, *J. Appl. Phys.* **1961**, *32*, 510.
[5] T. D. Lee, A. U. Ebong, *Renewable Sustainable Energy Rev.* **2017**, *70*, 1286.
[6] S. Bhattacharya, S. John, *APL Photonics* **2020**, *5*, 020902.
[7] P. R. Campbell, M. A. Green, *IEEE Trans. Electron Devices* **1986**, *33*, 1834.
[8] C. F. Guo, T. Sun, F. Cao, Q. Liu, Z. Ren, *Light: Sci. Appl.* **2014**, *3*, e161.
[9] M. L. Brongersma, Y. Cui, S. Fan, *Nat. Mater.* **2014**, *13*, 451.
[10] K. Li, S. Haque, A. Martins, E. Fortunato, R. Martins, M. J. Mendes, C. S. Schuster, *Optica* **2020**, *7*, 1377.
[11] Z. Yu, A. Raman, S. Fan, *Proc. Natl. Acad. Sci. USA* **2010**, *107*, 17491.
[12] A. De Vos, *J. Phys. D: Appl. Phys.* **1980**, *13*, 839.
[13] A. Tooghi, D. Fathi, M. Eskandari, *Sci. Rep.* **2020**, *10*, 18699.
[14] J. Werner, B. Niesen, C. Ballif, *Adv. Mater. Interfaces* **2018**, *5*, 1700731.
[15] J. M. Russo, D. Zhang, M. Gordon, S. Vorndran, Y. Wu, R. K. Kostuk, *Opt. Express* **2014**, *22*, A528.
[16] G. Huang, K. Wang, C. N. Markides, *Light: Sci. Appl.* **2021**, *10*, 28.
[17] W. Li, S. Buddhiraju, S. Fan, *Light: Sci. Appl.* **2020**, *9*, 68.
[18] S. De Wolf, B. Niesen, C. Ballif, *ACS Photonics* **2016**, *7*, 161.
[19] S. Albrecht, M. Saliba, P. Correa, F. Lang, L. Korte, R. Schlatmann, M. K. Nazeeruddin, A. Hagfeldt, M. Gra, *Energy Environ. Sci.* **2016**, *9*, 81.
[20] K. Xiao, Y. H. Lin, M. Zhang, R. D. J. Oliver, X. Wang, Z. Liu, X. Luo, J. Li, D. Lai, H. Luo, R. Lin, J. Xu, Y. Hou, H. J. Snaith, H. Tan, *Science* **2022**, *376*, 762.
[21] P. Caprioglio, J. A. Márquez, A. Belen, M. Vilches, E. Kasparavicius, C. Gollwitzer, T. Malinauskas, M. Jo, L. Korte, A. Abate, B. Stannowski, *Science* **2020**, *370*, 1300.
[22] J. A. Christians, P. A. M. Herrera, P. V. Kamat, *J. Am. Chem. Soc.* **2015**, *137*, 1530.
[23] S. De Wolf, J. Holovsky, S. J. Moon, P. Löper, B. Niesen, M. Ledinsky, F. J. Haug, J. H. Yum, C. Ballif, *J. Phys. Chem. Lett.* **2014**, *5*, 1035.
[24] J. Yang, B. D. Siempelkamp, D. Liu, T. L. Kelly, *ACS Nano* **2015**, *9*, 1955.
[25] R. Guo, D. Han, W. Chen, L. Dai, K. Ji, Q. Xiong, S. Li, L. K. Reb, M. A. Scheel, S. Pratap, N. Li, S. Yin, T. Xiao, S. Liang, A. L. Oechsle, C. L. Weindl, M. Schwartzkopf, H. Ebert, P. Gao, K. Wang, M. Yuan, N. C. Greenham, S. D. Stranks, S. V. Roth, R. H. Friend, P. Müller-Buschbaum, *Nat. Energy* **2021**, *6*, 977.
[26] R. Lin, J. Xu, M. Wei, Y. Wang, Z. Qin, Z. Liu, J. Wu, K. Xiao, B. Chen, S. M. Park, G. Chen, H. R. Atapattu, K. R. Graham, J. Xu, J. Zhu, L. Li, C. Zhang, E. H. Sargent, H. Tan, *Nature* **2022**, *603*, 73.
[27] M. I. Hossain, W. Qarony, S. Ma, L. Zeng, D. Knipp, Y. H. Tsang, *Nano-Micro Lett.* **2019**, *11*, 58.
[28] H. Li, Y. Wang, H. Gao, M. Zhang, R. Lin, P. Wu, K. Xiao, H. Tan, *eLight* **2022**, *2*, 21.
[29] F. Giordano, A. Abate, J. Pablo, C. Baena, M. Saliba, T. Matsui, S. H. Im, S. M. Zakeeruddin, M. K. Nazeeruddin, A. Hagfeldt, M. Graetzel, *Nat. Commun.* **2016**, *7*, 10379.
[30] O. Malinkiewicz, A. Yella, Y. H. Lee, G. M. Espallargas, M. Graetzel, M. K. Nazeeruddin, H. J. Bolink, *Nat. Photonics* **2014**, *8*, 128.
[31] J. Xie, K. Huang, X. Yu, Z. Yang, K. Xiao, Y. Qiang, X. Zhu, L. Xu, P. Wang, C. Cui, D. Yang, *ACS Nano* **2017**, *11*, 9176.
[32] W. J. Yin, T. Shi, Y. Yan, *Appl. Phys. Lett.* **2014**, *104*, 063903.
[33] D. L. Wang, H. J. Cui, G. J. Hou, Z. G. Zhu, Q. B. Yan, G. Su, *Sci. Rep.* **2016**, *6*, 18922.
[34] L. Zheng, Y. Ma, S. Chu, S. Wang, B. Qu, L. Xiao, Z. Chen, Q. Gong, Z. Wu, X. Hou, *Nanoscale* **2014**, *6*, 8171.
[35] W. Qarony, Y. A. Jui, G. M. Das, T. Mohsin, M. I. Hossain, S. N. Islam, *Am. J. Energy Res.* **2015**, *3*, 19.
[36] A. G. Martin, S. Pillai, *Nat. Photonics* **2012**, *6*, 130.
[37] H. A. Atwater, A. Polman, *Nat. Mater.* **2010**, *9*, 205.
[38] M. van Eerden, M. Jaysankar, A. Hadipour, T. Merckx, J. J. Schermer, T. Aernouts, J. Poortmans, U. W. Paetzold, *Adv. Opt. Mater.* **2017**, *5*, 1700151.
[39] C. M. Wolff, F. Zu, A. Paulke, L. P. Toro, N. Koch, D. Neher, *Adv. Mater.* **2017**, *29*, 1700159.

[40] Y. Li, W. Yan, Y. Li, S. Wang, W. Wang, Z. Bian, L. Xiao, Q. Gong, *Sci. Rep.* **2015**, *5*, 14485.
[41] K. Taretto, U. Rau, *Prog. Photovoltaics Res. Appl.* **2004**, *12*, 573.
[42] S. B. Mallick, M. Agrawal, P. Peumans, *Opt. Express* **2010**, *18*, 5691.
[43] C. T. Sah, K. A. Yamakawa, R. Lutwack, *IEEE Trans. Electron Devices* **1982**, *29*, 903.
[44] I. Karakasoglu, K. X. Wang, S. Fan, *ACS Photonics* **2015**, *2*, 883.
[45] T. Todorov, O. Gunawan, S. Guha, *Mol. Syst. Des. Eng.* **2016**, *1*, 370.
[46] A. Hoffmann, U. W. Paetzold, C. Zhang, T. Merdzhanova, A. Lambertz, C. Ulbrich, K. Bittkau, U. Rau, *Opt. Express* **2014**, *22*, A1270.
[47] J. Üpping, A. Bielawny, R. B. Wehrspohn, T. Beckers, R. Carius, U. Rau, S. Fahr, C. Rockstuhl, F. Lederer, M. Kroll, T. Pertsch, L. Steidl, R. Zentel, *Adv. Mater.* **2011**, *23*, 3896.
[48] A. Bielawny, J. Üpping, P. T. Miclea, R. B. Wehrspohn, C. Rockstuhl, F. Lederer, M. Peters, L. Steidl, R. Zentel, S. M. Lee, M. Knez, A. Lambertz, R. Carius, *Phys. Status Solidi A* **2008**, *205*, 2796.
[49] G. W. P. Adhyaksa, E. Johlin, E. C. Garnett, *Nano Lett.* **2017**, *17*, 5206.
[50] G. Coletti, S. L. Luxembourg, L. J. Geerligs, V. Rosca, A. R. Burgers, Y. Wu, L. Okel, M. Kloos, F. J. K. Danzl, M. Najafi, D. Zhang, I. Dogan, V. Zardetto, F. Di Giacomo, J. Kroon, T. Aernouts, J. Hüpkes, C. H. Burgess, M. Creatore, R. Andriessen, S. Veenstra, *ACS Energy Lett.* **2020**, *5*, 1676.
[51] L. Bai, B. Liu, J. Fan, D. Zhang, C. Wei, J. Sun, Y. Zhao, X. Zhang, *J. Power Sources* **2014**, *266*, 138.
[52] S. Novak, P. T. Lin, C. Li, C. Lumdee, J. Hu, A. Agarwal, P. G. Kik, W. Deng, K. Richardson, *ACS Appl. Mater. Interfaces* **2017**, *9*, 26990.
[53] P. Ji, C.-S. Park, S. Gao, S.-S. Lee, D.-Y. Choi, *Opt. Express* **2017**, *25*, 2153.
[54] M. T. Taschuk, M. M. Hawkeye, M. J. Brett, *Glancing Angle Deposition*, 3rd ed., Elsevier Ltd., New York **2009**.
[55] X. Sun, T. Lin, C. Ding, S. Guo, I. Ismail, Z. Wang, J. Wei, Q. Luo, J. Lin, D. Zhang, C. Q. Ma, *Org. Electron.* **2022**, *104*, 106475.
[56] G. K. Dalapati, S. Masudy-Panah, A. Kumar, C. C. Tan, H. R. Tan, D. Chi, *Sci. Rep.* **2015**, *5*, 17810.
[57] Y. Hou, E. Aydin, M. De Bastiani, C. Xiao, F. H. Isikgor, D. J. Xue, B. Chen, H. Chen, B. Bahrami, A. H. Chowdhury, A. Johnston, S. W. Baek, Z. Huang, M. Wei, Y. Dong, J. Troughton, R. Jalmood, A. J. Mirabelli, T. G. Allen, E. Van Kerschaver, M. I. Saidaminov, D. Baran, Q. Qiao, K. Zhu, S. De Wolf, E. H. Sargent, *Science* **2020**, *367*, 1135.
[58] S. Altazin, L. Stepanova, J. Werner, B. Niesen, C. Ballif, B. Ruhstaller, *Opt. Express* **2018**, *26*, A579.
[59] X. Wang, M. R. Khan, J. L. Gray, M. A. Alam, M. S. Lundstrom, *IEEE J. Photovoltaics* **2013**, *3*, 737.
[60] G. Yu, C. Shou, Z. Yang, H. He, Y. Zhang, *Sol. Energy* **2021**, *228*, 226.
[61] W. Qarony, M. I. Hossain, R. Dewan, S. Fischer, V. B. Meyer-Rochow, A. Salleo, D. Knipp, Y. H. Tsang, *Adv. Theory Simul.* **2018**, *1*, 1800030.
[62] L. J. Phillips, A. M. Rashed, R. E. Treharne, J. Kay, P. Yates, I. Z. Mitrovic, A. Weerakkody, S. Hall, K. Durose, *Data Brief* **2015**, *5*, 926.
[63] S. E. Baroni, *Phys. Rev. B* **1983**, *27*, 985.
[64] S. Zhong, W. Wang, M. Tan, Y. Zhuang, W. Shen, *Adv. Sci.* **2017**, *4*, 1700200.
[65] M. J. Yun, Y. H. Sim, S. I. Cha, D. Y. Lee, *Sci. Rep.* **2019**, *9*, 10273.
[66] Y. A. Cengel, *McGraw-Hill* **2004**, *4*, 874.
[67] S. Limpert, S. Bremner, H. Linke, *New J. Phys.* **2015**, *17*, 095004.
[68] F. H. Alharbi, S. Kais, *Renewable Sustainable Energy Rev.* **2015**, *43*, 1073.
[69] R. A. Sinton, R. M. Swanson, *IEEE Trans. Electron Devices* **1987**, *34*, 1380.
[70] E. Yablonovitch, T. Gmitter, *Appl. Phys. Lett.* **1986**, *49*, 587.
[71] G. J. A. H. Wetzelaer, M. Scheepers, A. M. Sempere, C. Momblona, J. Ávila, H. J. Bolink, *Adv. Mater.* **2015**, *27*, 1837.
[72] J. W. Lee, Y. T. Hsieh, N. De Marco, S. H. Bae, Q. Han, Y. Yang, *J. Phys. Chem. Lett.* **2017**, *8*, 1999.
[73] M. Moradbeigi, M. Razaghi, *Sci. Rep.* **2022**, *12*, 6733.
[74] S. E. Köhnen, S. Albrecht, *Sustainable Energy Fuels* **2019**, *3*, 1995.
[75] J. Wang, *EcoMat* **2022**, e12263.